

# Gravitational odd-parity perturbation of a Horndeski hairy black hole: quasinormal mode and parameter constraint

Zhen-Hao Yang,<sup>1</sup> Yun-He Lei,<sup>1</sup> Xiao-Mei Kuang,<sup>1,\*</sup> and Bin Wang<sup>1,2</sup>

<sup>1</sup>*Center for Gravitation and Cosmology, College of Physical Science and Technology, Yangzhou University, Yangzhou, 225009, China*

<sup>2</sup>*Shanghai Frontier Science Center for Gravitational Wave Detection, Shanghai Jiao Tong University, Shanghai 200240, China*

In the binary black hole coalescence, the gravitational wave emitted at the ringdown stage can be well described within the black hole perturbation theory, where the quasinormal modes (QNMs) become the important ingredient in modeling the pattern wave form. In general relativity (GR), the QNMs can be obtained from solving the Regge-Wheeler equation in static black hole, while in Horndeski gravity, the metric perturbation equation can be simplified into a modified Regge-Wheeler equation from the perturbed action. In this paper, we calculate the QNMs frequencies of the gravitational odd-parity perturbation of a specific hairy black hole in Horndeski gravity with the use of the matrix method and pseudo spectral method. Our results indicate that such a Horndeski hairy black hole is stable under the odd perturbation, which is also verified by the time evolution of the perturbation. In particular, we find that for a certain range of the Horndeski hair, the  $\ell > 2$  modes become the long-lived mode instead of  $\ell = 2$  mode in GR. Then, we use the ringdown QNMs to preliminarily investigate the signal-to-noise-ratio (SNR) rescaled measurement error of the Horndeski hair. We obtained significant effects of the angular momentum and overtone on the error bound of the hairy parameter. We hope that our findings could inspire more theoretical and phenomenal work on the test of no-hair theorem of black hole from gravitational wave physics.

## Contents

<b>I. Introduction</b>	2
<b>II. Equation of motion for the odd-parity perturbation</b>	3
A. Review on the action and Horndeski hairy black hole	3
B. Odd-parity perturbation and modified Regge-Wheeler equation	5
<b>III. Quasinormal mode</b>	7
A. Preparation	7
B. Numerical results	8
<b>IV. Hairy parameter estimation by detection of ringdown wave</b>	10
A. Single-mode parameter estimation	11
B. Two-modes parameter estimation	12
<b>V. Conclusions and discussions</b>	14
<b>Acknowledgments</b>	15
<b>References</b>	15

---

\*Electronic address: [xmeikuang@yzu.edu.cn](mailto:xmeikuang@yzu.edu.cn) (corresponding author)

## I. INTRODUCTION

Testifying the no hair theorem of black hole is important to test the nature of gravity and more fundamental physics, which inevitably requires us to explore the strong gravity regime. The potential ways of seeking the black hole hair are to investigate the imprints of hair on the gravitational wave (GW) and on the shadow from the black hole. Recent GW observations from the merger of black holes or other compact objects [1–3] and black hole shadows from supermassive black holes [4, 5] open new era of exploring physics about strong gravity regime, which trigger extensive investigation about the prints of hair on the GW and shadows. The studies on testing the no hair theorem with Event Horizon Telescope (EHT) observations can refer to, for examples, the literatures [6–10], but in this scenario, a universal challenge is the high precision in detecting the print of hair on black hole shadow. This is because the hair should directly affect the orbits very near the black hole horizon, but the photon ring is still far away from the horizon. GWs generated from extreme mass ratio inspiral (EMRI) and ringdown stage in binary black hole coalescence are potential tools to seek the black hole hair [11, 12]. In the stage of EMRI the hair will influence the inspiraling orbits and energy radiation [13–22], while in ringdown stage, the hair will characterize the ringdown GW wave [23–27]. Therefore, it is important to concern both cases to completely trace the imprint of black hole hair on the GWs.

Introducing scalar field into the action of a gravitational sector is a natural way to construct black hole with scalar hair. Among the numerous gravity theories, the Horndeski gravity containing higher derivatives of a scalar field  $\phi$  and metric tensor  $g_{\mu\nu}$  have retained lots of attentions, since it possesses at most second-order differential field equations so as to be free of Ostrogradski instabilities [28]. Various observational constraints or bounds on Horndeski theories have been explored in [29–35] and references therein. Horndeski gravity is also active in the cosmological and astrophysical communities since it has significant consequences in describing the accelerated expansion and other interesting features [36]. Moreover, since Horndeski theory contains a scalar field, and similar to GR it has diffeomorphism invariance and second-order field equations, so it also provides a natural platform to testify the no-hair theorem of black hole. In fact, hairy black holes in Horndeski gravity have been widely studied, for instances, the radially dependent scalar field [37–50] and the time-dependent scalar field [51–56]. The hairy solution with a scalar hair in linear time dependence was initially ruled out due to instability [57], however, another novel solution with a time-dependent scalar hair was recently constructed [58] and found to be stable [59]. The stability conditions for a similar time-dependent background solution beyond Horndeski theories was also addressed in [60]. Moreover, it was demonstrated in [61], that the no-hair theorem cannot be hold when a Galileon field is coupled to gravity, but the static spherical solution only admits trivial Galileon profile.

An interesting new development in the examination of no-hair theorem in Horndeski theories is that the shift-symmetric Horndeski theory and beyond with the action [62]

$$S = \int d^4x \sqrt{-g} \left[ Q_2 + Q_3 \square \phi + Q_4 R + Q_{4,\chi} \left( (\square \phi)^2 - (\nabla^\mu \nabla^\nu \phi)(\nabla_\mu \nabla_\nu \phi) \right) + Q_5 G_{\mu\nu} \nabla^\mu \nabla^\nu \phi - \frac{1}{6} Q_{5,\chi} \left( (\square \phi)^3 - 3(\square \phi)(\nabla^\mu \nabla^\nu \phi)(\nabla_\mu \nabla_\nu \phi) + 2(\nabla_\mu \nabla_\nu \phi)(\nabla^\nu \nabla^\gamma \phi)(\nabla_\gamma \nabla^\mu \phi) \right) \right] \quad (1)$$

allow static and asymptotically flat black holes with a nontrivial static scalar field. In the above action,  $g$  is the determinant of the metric and  $R$  is the Ricci scalar.  $\chi = -\partial^\mu \phi \partial_\mu \phi / 2$  is the canonical kinetic term,  $Q_i$  ( $i = 2, 3, 4, 5$ ) are arbitrary functions of the scalar field  $\phi$  and the kinetic term  $\chi$  and  $Q_{i,\chi} \equiv \partial Q_i / \partial \chi$ . In particular, a static hairy black hole in a specific quartic Horndeski theory, which includes an additional *log*-term deforming from the standard Schwarzschild black hole, has been constructed in [63]. This Horndeski hairy black hole soon attracts plenty of attentions, and various theoretical and observational phenomena have been disclosed, for instances, thermodynamic and weak gravitational lensing [64, 65], the strong gravitational lensing [66], shadow constraint from EHT observation [67, 68], superradiant properties in its rotating counterpart [69, 70], photon rings in the black hole image [71, 72] and precessing and periodic orbits [73]. These studies disclosed the novel properties brought by the Horndeski hair, differentiating from the Schwarzschild black hole in GR, which are helpful to understand the gravitational structure of the specific theory.

Another significant question concerning this Horndeski hairy black hole is its stability. It was addressed in [64] that the Horndeski hairy black hole is thermodynamically preferred. Later, we also disclosed its dynamical stability under various external massless perturbed fields including the scalar field, electromagnetic field and Dirac field in [74]. However, up to now, its dynamical stability has not been completely investigated. To promote this topic, we have to perturb the metric itself and study the linear mode as a first important step, in which the modes of a spherically symmetric black holes usually can be classified into the even-parity (polar) modes and odd-parity (axial) modes.

On the other hand, considering that the gravitational waves radiated from black hole coalescence contain rich information about the nature of spacetime, it is significant to study the gravitational wave signatures of such hairy black hole. In particular, the ringdown wave, as the associated gravitational emission at the late time of binary black hole coalescence, is expected to be modeled by the superposition of exponentially damped sinusoidal signals. In this stage, the QNMs could be the key observable in constructing the patterns of such signal and therefore could be used to examine the no-hair theorem due to its highly dependency on the black hole parameter. Thus, the first step in this direction is to study their QNMs, which describes the ringdown stage after the binary black holes merger [75]. The QNMs are the eigenmodes of a dissipative system, which inherently reflect the influence of all the system's parameters. Consequently, if a black hole acquires an additional Horndeski hair, its QNMs will naturally encode the characteristics of this scalar hair. Due to the dissipative nature of the system, the frequencies of QNMs are usually have two parts: the real part and the imaginary part, the former of which gives the frequency of vibration while the latter describes the damping timescale. The readers can refer to the reviews [76–78] for more details.

Thus, motivated from the above aspects, in this paper we will consider the dynamic of the gravitational odd-parity perturbations of a specific Horndeski hairy black hole. We expect that it has a simpler spectrum than the even-parity modes because they do not contain the perturbations of the scalar field in contrast to the latter. We shall study the time domain evolution and QNMs frequencies for the odd-parity perturbations, then further answer the question whether the hairy black hole is stable under such perturbations. Moreover, in order to check the imprint of Horndeski hair on the GW in ringdown stage and give some insight into the test of no hair theorem, we will use the yielding QNMs data to construct the ringdown GW wave form and further calculate the Fisher information matrix (FIM) [79] to obtain the measurement error of the detection of the Horndeski hair.

This paper is organized as follows. In section II, we derive the modified Regge-Wheeler equation in a specific hairy black hole. In section III, we numerically solve the master equation, and extract the QNMs frequencies of the gravitational odd perturbation. We analyze the effects of scalar hair  $Q$ , the angular number  $\ell$ , and the overtones  $n$  on the QNM frequencies. In section IV, we first briefly review the waveform modeling in the ringdown stage, and then investigate the detectability of the specific Horndeski hair by calculating the error bound in cases with single-mode and mixed-mode estimations. Section V concludes with our key findings and outlooks for future work. Throughout the paper, we will set  $c = \hbar = G = 1$  unless we restate it.

## II. EQUATION OF MOTION FOR THE ODD-PARITY PERTURBATION

### A. Review on the action and Horndeski hairy black hole

Horndeski gravity is the most general scalar-tensor field theory in four dimensions which possesses second-order field equations [28]. In these subsection, we shall focus on a special subclass of Horndeski theory and review the static hairy black hole constructed in [63]. The action is

$$S = \int d^4x \sqrt{-g} [Q_2 + Q_3 \square \phi + Q_4 R + Q_{4,\chi} ((\square \phi)^2 - (\nabla^\mu \nabla^\nu \phi)(\nabla_\mu \nabla_\nu \phi))], \quad (2)$$

which is obtained by setting  $Q_5 = 0$  in the general action (1). From the above action, we can vary it with respect to  $g^{\mu\nu}$  to obtain the field equation

$$\begin{aligned}
Q_4 G_{\mu\nu} = & \frac{1}{2}(Q_{2,\chi} \phi_{,\mu} \phi_{,\nu} + Q_2 g_{\mu\nu}) + \frac{1}{2} Q_{3,\chi} (\phi_{,\mu} \phi_{,\nu} \square \phi - g_{\mu\nu} \chi_{,\alpha} \phi^{,\alpha} + \chi_{,\mu} \phi_{,\nu} + \chi_{,\nu} \phi_{,\mu}) \\
& - Q_{4,\chi} \left\{ \frac{g^{\mu\nu}}{2} [(\square \phi)^2 - (\nabla_\alpha \nabla_\beta \phi)(\nabla^\alpha \nabla^\beta \phi) - 2R_{\sigma\gamma} \phi^{,\sigma} \phi^{,\gamma}] - \nabla_\mu \nabla_\nu \phi \square \phi + \nabla_\gamma \nabla_\mu \phi \nabla^\gamma \nabla_\nu \phi \right. \\
& \left. - \frac{R}{2} \phi_{,\mu} \phi_{,\nu} + R_{\sigma\mu} \phi^{,\sigma} \phi_{,\nu} + R_{\sigma\nu} \phi^{,\sigma} \phi_{,\mu} + R_{\sigma\nu\gamma\mu} \phi^{,\sigma} \phi^{,\gamma} \right\} \\
& - Q_{4,\chi} \left\{ g_{\mu\nu} (\chi_{,\alpha} \phi^{,\alpha} \square \phi + \chi_{,\alpha} \chi^{,\alpha}) + \frac{1}{2} \phi_{,\mu} \phi_{,\nu} \times (\nabla_\alpha \nabla_\beta \phi \nabla^\alpha \nabla^\beta \phi - (\square \phi)^2) - \chi_{,\mu} \chi_{,\nu} \right. \\
& \left. - \square \phi (\chi_{,\mu} \phi_{,\nu} + \chi_{,\nu} \phi_{,\mu}) - \chi_{,\gamma} [\phi^{,\gamma} \nabla_\mu \nabla_\nu \phi - (\nabla^\gamma \nabla_\mu \phi) \phi_{,\nu} - (\nabla^\gamma \nabla_\nu \phi) \phi_{,\mu}] \right\}, \tag{3}
\end{aligned}$$

and also obtain the four-current as

$$\begin{aligned}
j^\nu = & \frac{1}{\sqrt{-g}} \frac{\delta S}{\delta(\phi_{,\mu})} \\
= & -Q_{2,\chi} \phi^{,\nu} - Q_{3,\chi} (\phi^{,\nu} \square \phi + \chi^{,\nu}) - Q_{4,\chi} (\phi^{,\nu} R - 2R^{\nu\sigma} \phi_{,\sigma}) \\
& - Q_{4,\chi} \left\{ \phi^{,\nu} [(\square \phi)^2 - (\nabla_\alpha \nabla_\beta \phi)(\nabla^\alpha \nabla^\beta \phi)] + 2(\chi^{,\nu} \square \phi - \chi_{,\mu} \nabla^\mu \nabla^\nu \phi) \right\}. \tag{4}
\end{aligned}$$

In order to construct an exact solution to the above sector, we first consider the ansatz

$$\phi = \phi(r), \tag{5}$$

$$ds^2 = -A(r)dt^2 + \frac{dr^2}{B(r)} + r^2(d\theta^2 + \sin^2 \theta d\varphi^2), \tag{6}$$

such that the only non-vanishing component of the current takes the form

$$j^r = -Q_{2,\chi} B\phi' - Q_{3,\chi} \frac{(4A + rA')}{2rA} B^2 \phi'^2 + 2Q_{4,\chi} \frac{B}{r^2 A} [(B-1)A + rBA'] \phi' - 2Q_{4,\chi} \frac{B^3(A + rA')}{r^2 A} \phi'^3, \tag{7}$$

where the prime means the derivative with respect to the coordinate  $r$ . Then, one can further fix

$$Q_2 = \alpha_{21}\chi + \alpha_{22}(-\chi)^{\omega_2}, \quad Q_3 = \alpha_{31}(-\chi)^{\omega_3}, \quad Q_4 = \frac{1}{8\pi} + \alpha_{42}(-\chi)^{\omega_4}, \tag{8}$$

and set  $\alpha_{21} = \alpha_{31} = 0$ ,  $\omega_2 = \frac{3}{2}$  and  $\omega_4 = \frac{1}{2}$  to obtain a solution with non-trivial scalar field. Subsequently, imposing the condition  $\lim_{r \rightarrow \infty} j^r = 0$  yields

$$\phi' = \pm \frac{2}{r} \sqrt{\frac{-\alpha_{42}}{3B\alpha_{22}}}, \tag{9}$$

and then solving the field equation gives

$$A(r) = B(r) = 1 - \frac{2M}{r} + \frac{Q}{r} \ln\left(\frac{r}{2M}\right) \quad \text{and} \quad Q = 8\pi \left(\frac{2}{3}\right)^{3/2} \alpha_{42} \sqrt{-\frac{\alpha_{42}}{\alpha_{22}}}, \tag{10}$$

where  $M$  and  $Q$  are integral constants. It is noticed from (10) that  $\alpha_{42}$  and  $\alpha_{22}$  should have different signs to guarantee that the scalar field is real.

Thus, the subclass Horndeski theory with the action (2) with some specific settings admits a Horndeski hairy black hole with the metric [63]

$$ds^2 = -f(r)dt^2 + \frac{dr^2}{f(r)} + r^2(d\theta^2 + \sin^2 \theta d\varphi^2) \quad \text{with} \quad f(r) = 1 - \frac{2M}{r} + \frac{Q}{r} \ln\left(\frac{r}{2M}\right), \tag{11}$$

in which the hairy term appears as a *log* term deforming the standard Schwarzschild black hole. Similarly, the integral constants  $M$  and  $Q$  are related with the mass and hairy charge of the black hole. It is obvious that the metric is

asymptotically flat since  $f(r)|_{r \rightarrow \infty} = 1$ . Let us briefly analyze the structure of the hairy metric (11). For arbitrary  $Q$ ,  $r = 0$  is an intrinsic singularity as the curvature scalar is singular, and  $f(r) = 0$  always admits the solution  $r_+ = 2M$ . In addition, (i) when  $Q \rightarrow 0$ , the metric reduces to Schwarzschild case. (ii) When  $Q > 0$ ,  $r_+ = 2M$  is the unique root to  $f(r) = 0$ , so it has a unique horizon, i.e., the event horizon for the hairy black hole which resemble Schwarzschild black hole. (iii) While for  $-2M < Q < 0$ ,  $f(r) = 0$  gives two distinguishable positive real roots: the larger one is  $r_+ = 2M$  denoting the position of event horizon, and the smaller one  $r_-$  denotes the Cauchy horizon which is smaller than the event horizon. The Cauchy horizon  $r_-$  increases as  $Q$  decreases, and finally coincides with  $r_+$  when  $Q = -2M$ , indicating the extreme case.

### B. Odd-parity perturbation and modified Regge-Wheeler equation

In this subsection, we will consider the gravitational perturbation to the Horndeski hairy black hole (11). We will focus on the odd-parity perturbation in linear order, where we can ignore the coupling between the even-parity metric perturbation and the perturbation of energy momentum tensor from the scalar field, because both of them decouple from the odd-parity perturbation. The gravitational perturbation of general spherically symmetric black holes in Horndeski gravity was well addressed in [80, 81], based on which we shall derive the modified Regge-Wheeler equation for the odd-parity perturbation of the current hairy black hole.

Under the Regge-Wheeler gauge [82], the odd perturbation to the background metric is

$$h_{\mu\nu, \ell m}^{\text{odd}} = \begin{pmatrix} 0 & 0 & 0 & h_0(r, t) \\ 0 & 0 & 0 & h_1(r, t) \\ 0 & 0 & 0 & 0 \\ h_0(r, t) & h_1(r, t) & 0 & 0 \end{pmatrix} \sin \theta \partial_\theta Y_{\ell m} \quad (12)$$

where the spherical harmonics can be replaced by Legendre polynomials by setting the azimuthal number  $m = 0$  without loss of generality, i.e.  $Y_{\ell m}|_{m=0} = \sqrt{\frac{2\ell+1}{4\pi}} P_\ell(\cos \theta)$ , because the background hairy metric is spherical symmetric. By substituting the Horndeski hairy metric (11) and the perturbation (12) into the action (2), we can obtain a second order action as

$$S^{(2)} = \int dt dr \left[ a_1 h_0^2 + a_2 h_1^2 + a_3 \left( \dot{h}_1^2 + h_0'^2 - 2\dot{h}_1 h_0' + \frac{4}{r} \dot{h}_1 h_0 \right) \right] \quad (13)$$

in which we have integrated out the coordinates  $\theta$  and  $\phi$ . Here the dot and prime denote the derivative with respect to  $t$  and  $r$ , respectively, and the coefficients are expressed as

$$a_1 = \frac{\ell(\ell+1)}{4r^2} \left[ [4r(Q_4 - 2\chi Q_{4,\chi})]' + \frac{2(\ell-1)(\ell+2)}{f} Q_4 \right], \quad (14)$$

$$a_2 = -\frac{\ell(\ell+1)(\ell-1)(\ell+2)f}{2r^2} (Q_4 - 2\chi Q_{4,\chi}), \quad (15)$$

$$a_3 = \frac{\ell(\ell+1)}{2} (Q_4 - 2\chi Q_{4,\chi}). \quad (16)$$

To proceed, we introduce a new auxiliary field [83, 84]

$$\Psi(r, t) = \frac{\sqrt{2}r(Q_4 - 2\chi Q_{4,\chi})}{\sqrt{Q_4}} \left( \dot{h}_1 - h_0' + \frac{2h_0}{r} \right) \quad (17)$$

such that under the tortoise coordinate  $r_* = \int \frac{dr}{f}$ , the second order action (13) can be reduced as

$$S^{(2)} = \frac{\ell(\ell+1)}{4(\ell-1)(\ell+2)} \int dt dr_* \left[ \frac{Q_4}{Q_4 - 2\chi Q_{4,\chi}} \left( \frac{d\Psi}{dt} \right)^2 - \left( \frac{d\Psi}{dr_*} \right)^2 - V(r) \Psi^2 \right] \quad (18)$$

where the potential  $V(r)$  takes the form

$$V(r) = \ell(\ell+1) \frac{fQ_4}{r^2(Q_4 - 2\chi Q_{4,\chi})} - \frac{r^3}{2} \left( \frac{f^2}{r^4} \right)' - \frac{r^4 Q_4^2}{4Q_4'} \left( \frac{f^2 Q_4'^2}{r^4 Q_4^3} \right)' - \frac{2fQ_4}{r^2(Q_4 - 2\chi Q_{4,\chi})}. \quad (19)$$

It is obvious from (18) that the second order actions is only well-defined for  $\ell \geq 2$  but not for the modes  $\ell = 0$  and  $\ell = 1$  which are in fact not dynamical.

Taking the variation of the action (18), we can obtain the equation of motion

$$\left( \frac{d}{dr_*^2} - \frac{Q_4}{Q_4 - 2\chi Q_{4,\chi}} \frac{d}{dt^2} - V(r) \right) \Psi = 0. \quad (20)$$

which is the modified Regge-Wheeler equation for the Horndeski hairy black hole (11) in the subclass of Horndeski theory with the action (2). Solving this equation with proper boundary conditions allows us to extract the spectrum of the odd-parity perturbation and to further analyze the stability of the hairy black hole and other related properties, which will be discussed in the next sections. Before closing this section, we will briefly examine the radial speed of gravitational wave in the current model, which is also known as the speed of perturbation propagating along the the radial direction. This speed is defined by the coefficient of  $\frac{d}{dt^2}$  as

$$c_r^2 = \frac{Q_4 - 2\chi Q_{4,\chi}}{Q_4} = \left( 1 + \frac{3Q}{2r} \right)^{-1}. \quad (21)$$

It is obvious that the scalar charge  $Q$  indeed cause the deviation of  $c_r^2$  from the vacuum light speed, i.e. the result in GR. Equation (21) shows that the Laplacian instability caused by  $c_r^2 < 0$  may occur. Considering that it is a monotonically increasing function of the radial coordinate  $r$ , so in order to avoid such instability, a condition for keeping a positive  $c_r^2$  must be imposed at least at the event horizon, i.e.

$$Q > -\frac{2}{3}r_+, \quad (22)$$

which is consistent with the stability condition addressed in [80, 84]. Moreover, to illustrate how the hairy parameter affect the radial propagation speed of the odd perturbation, we plot FIG.1 which shows that propagation speed can be larger or smaller than the vacuum light speed depending on the hairy charge.

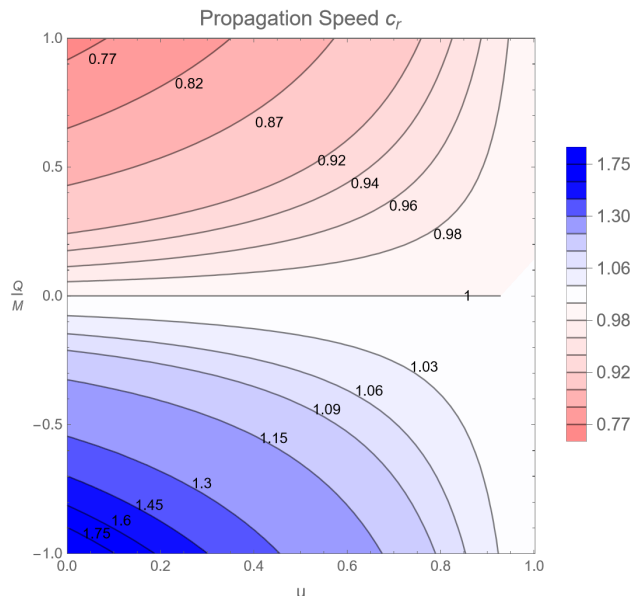


FIG. 1: The radial propagation speed of odd perturbation, here we have fixed  $M = 1/2$  and defined  $u = 1 - \frac{r_+}{r}$ .

### III. QUASINORMAL MODE

Recalling the Horndeski hairy black hole (11), the modified Regge-Wheeler equation can be rewritten as

$$\left[ \frac{d}{dr_*^2} - \left(1 + \frac{3Q}{2r}\right) \frac{d}{dt^2} - V(r) \right] \Psi = 0 \quad \text{with} \quad (23)$$

$$V(r) = \frac{f^2(27Q^2 + 48Qr + 32r^2)}{4r^2(3Q + 2r)^2} + \left(1 + \frac{3Q}{2r}\right) f \left[ \frac{(\ell - 2)(\ell + 1)}{r^2} - \frac{f'(3Q + 4r)}{(3Q + 2r)^2} \right], \quad (24)$$

which returns to the Regge-Wheeler potential [82] when the Horndeski hair vanishes. Since the explicit expression for the wave-like equation is clearly established, we are now in a position to solve the equation and extract the dynamical properties for the odd-parity perturbation, which allows us to work in both time and frequency domains.

#### A. Preparation

Firstly, we will give the method and boundary conditions in our numerical calculations to solve (23) from two aspects.

- **In time domain**, we shall work in tortoise coordinate grids and apply the finite difference method (the readers may refer to [74, 85] for more details) to discretize the radial coordinate  $r = r(r_*) = r(j\Delta r_*) = r_j$ , thus the perturbation and the potential are discretized as  $\Psi(t, r) = \Psi(i\Delta t, j\Delta r_*) = \psi_{i,j}$  and  $V(r) = V(j\Delta r_*) = V_j$ . Then we use the central difference to discretize the derivative of the perturbation and rewrite the equation (23) into an iterative equation

$$\Psi_{i+1,j} = \frac{\Delta t^2 (\Psi_{i,j-1} - 2\Psi_{i,j} + \Psi_{i,j+1})}{\left(1 + \frac{3Q}{2r_j}\right) \Delta r_*^2} - \Delta t^2 V_j \Psi_{i,j} + 2\Psi_{i,j} - \Psi_{i-1,j}. \quad (25)$$

By imposing the initial conditions  $\Psi_{i<0,j} = 0$ ,  $\Psi_{0,j} = \exp[-\frac{(r_j-18)^2}{2}]$ , and setting  $\frac{\Delta t}{\Delta r_*} = \frac{0.05}{0.1} = \frac{1}{2}$  to satisfy the Von Neumann stability, we can finally solve the evolution of the odd perturbation from the iterative equation. The evolutionary profile of the perturbation typically includes an initial outburst, a damped oscillation, and a late-time tail, from which one can compare the damping time of the perturbation in varying black hole parameters and roughly predict the (in)stability of the background spacetime.

- **In frequency domain**, we shall factor out the time dependency of the perturbation by separating  $\Psi(t, r) = e^{-i\omega t} R(r)$  in (23), which yields a general eigenvalue equation

$$\left[ \frac{d}{dr_*^2} + \left(1 + \frac{3Q}{2r}\right) \omega^2 - V(r) \right] R(r) = 0. \quad (26)$$

The boundary conditions for the QNMs solution are ingoing at the horizon  $R(r \rightarrow r_+) \sim e^{-i\sqrt{1+\frac{3Q}{2r_+}}\omega r_*}$  and outgoing at the infinity  $R(r \rightarrow \infty) \sim e^{i\omega r_*}$ , respectively. Thus, once the black hole parameters (for instance, the mass  $M$  and the hairy charge  $Q$ ) are fixed, the eigenvalues could be solved as an infinite series of complex numbers, which are the so-called QNM frequencies. Similar to the normal modes, the real part of the QNMs represents the physical oscillation angular frequency, but they differ from the normal modes by having a non-vanishing imaginary part that represents the exponential damping of the perturbation in a dissipating system.

We shall employ the pseudo-spectral method and the matrix method to solve the master equation (26) and determine the QNMs for the gravitational odd modes of the Horndeski black hole. Since both algorithms are widely used in studying of black hole spectroscopy, here we will not review the main steps, and readers may refer to [86] for the pseudo-spectral method and [87] for the matrix method, respectively. It is noticed that

due to the  $\log$  term in the metric function, a redefinition of the radial wave function is crucial when using both methods, as we have addressed in appendix B of our previous work [74]. Similar processes will be done in the current numerical calculations.

Following the above preparation, we shall show our numerical results of the eigenfrequencies of the QNMs and time evolution of perturbed field in next subsection. In our numeric, we find that as the hairy parameter goes closer to the extremal case, the precision of our calculation becomes worse and even the code may break down. So, we shall focus on the parameter regime  $-M \leq Q \leq M$ , and for simplicity, we also rescale the Horndeski charge into the dimensionless  $\tilde{Q} = Q/M$  in the calculations.

## B. Numerical results

The QNM frequencies with nodes  $n = 0, 1$  for the selected hairy charges obtained from the pseudo-spectral method and the matrix method are listed in TABLE I, where we also pledge the accuracy of the results by evaluating their relative error. It is shown that for each mode, when  $|\tilde{Q}|$  is small, both methods achieve high accuracy in the nodes  $n = 0$  and  $1$ , and the results are in good agreement with each other at least at the order of  $10^{-6}$  or even better.

		$\tilde{Q} = 0$	$\tilde{Q} = -0.5$	$\tilde{Q} = -1$
$\ell = 2$	$n = 0$	0.747343 - 0.177925 i	0.679390 - 0.163833 i	0.617493 - 0.153284 i
		0.747343 - 0.177925 i	0.679390 - 0.163833 i	0.617495 - 0.153284 i
	error%	0	0	0.000324 + 0 i
	$n = 1$	0.693422 - 0.547830 i	0.623772 - 0.504366 i	0.573986 - 0.481454 i
		0.693420 - 0.547829 i	0.623768 - 0.504368 i	0.574023 - 0.481421 i
error%	-0.000288 + 0.000183 i	-0.000641 - 0.000397 i	0.006446 + 0.006854 i	
$\ell = 3$	$n = 0$	1.198887 - 0.185406 i	1.078947 - 0.167580 i	0.955588 - 0.150350 i
		1.198887 - 0.185406 i	1.078947 - 0.167580 i	0.955587 - 0.150349 i
	error%	0	0	-0.000105 + 0.000665 i
	$n = 1$	1.165288 - 0.562596 i	1.046267 - 0.508376 i	0.929446 - 0.458644 i
		1.165288 - 0.562596 i	1.046269 - 0.508377 i	0.929442 - 0.458645 i
error%	0	0.000182 - 0.000240 i	-0.000430 - 0.000218 i	
$\ell = 4$	$n = 0$	1.618357 - 0.188328 i	1.451873 - 0.169314 i	1.274651 - 0.149665 i
		1.618357 - 0.188328 i	1.451873 - 0.169314 i	1.274651 - 0.149666 i
	error%	0	0	0. - 0.000668 i
	$n = 1$	1.593263 - 0.568668 i	1.427902 - 0.511200 i	1.255580 - 0.452830 i
		1.593263 - 0.568669 i	1.427904 - 0.511200 i	1.255583 - 0.452831 i
error%	0	0.000140 + 0 i	0.000221 - 0.000301 i	

TABLE I: The QNMs obtained by pseudo-spectral (upper) and matrix (lower) method of the hairy black hole, for  $\ell = 2, 3, 4$  and  $n = 0, 1$ . The relative errors are also shown below each mode, defined by  $\Delta_k = \frac{\text{Matrix}(\omega_k) - \text{Pseudospectral}(\omega_k)}{\text{Pseudospectral}(\omega_k)} 100\%$  with  $k = \text{Re}, \text{Im}$ .

In order to explicitly see the effect of the Horndeski hair on the QNMs, we plot the frequencies with first three nodes as functions of hairy charge for  $\ell = 2, 3, 4$  modes in FIG.2. For all the modes except  $\ell = n = 2$  (the blue solid curves), the imaginary part increases while the real part decreases as the scaled hairy parameter becomes smaller, but the imaginary part, related with the damping rates by  $-Im(\omega) \sim 1/\tau$ , is always negative. For one thing, this makes the odd perturbation always decay and therefore the black hole can remain stable in the range of  $\tilde{Q} \in \{-1, 1\}$ . For another, this causes the odd perturbation to have a longer damping time. This is consistent with the phenomena we can observe in time domain (FIG.3), that the ringing stage of the perturbation with  $\tilde{Q} = -1$  is always more lasting than that for other parameters. In addition, for the tendency of the real part  $Re(\omega)$ , it can be obviously seen that the decreasing of  $\tilde{Q}$  can suppress the oscillation of the odd perturbation, which corresponds to sparse ringing for smaller  $\tilde{Q}$  in time domain. Regarding the effects of angular momentum and overtone, we find that the influence of  $\ell$  on the  $Im(\omega)$  is much slighter than that of  $n$ . Moreover, it is interesting to notice that as  $\tilde{Q}$  becomes negative enough, the long-lived modes with the same node are replaced by the  $\ell > 2$  modes, instead of the typical  $\ell = 2$  mode in the usual scenario. For the higher overtone, the  $Im(\omega)$  of  $\ell = 2$  mode is highly suppressed by the negative hairy charge. In



particular, both  $Im(\omega)$  and  $Re(\omega)$  of the node  $n = 2$  for  $\ell = 2$  mode will slightly change the tendency at  $\tilde{Q} \sim -0.8$ , indicating novel effects of the hairy charge on the higher overtones.

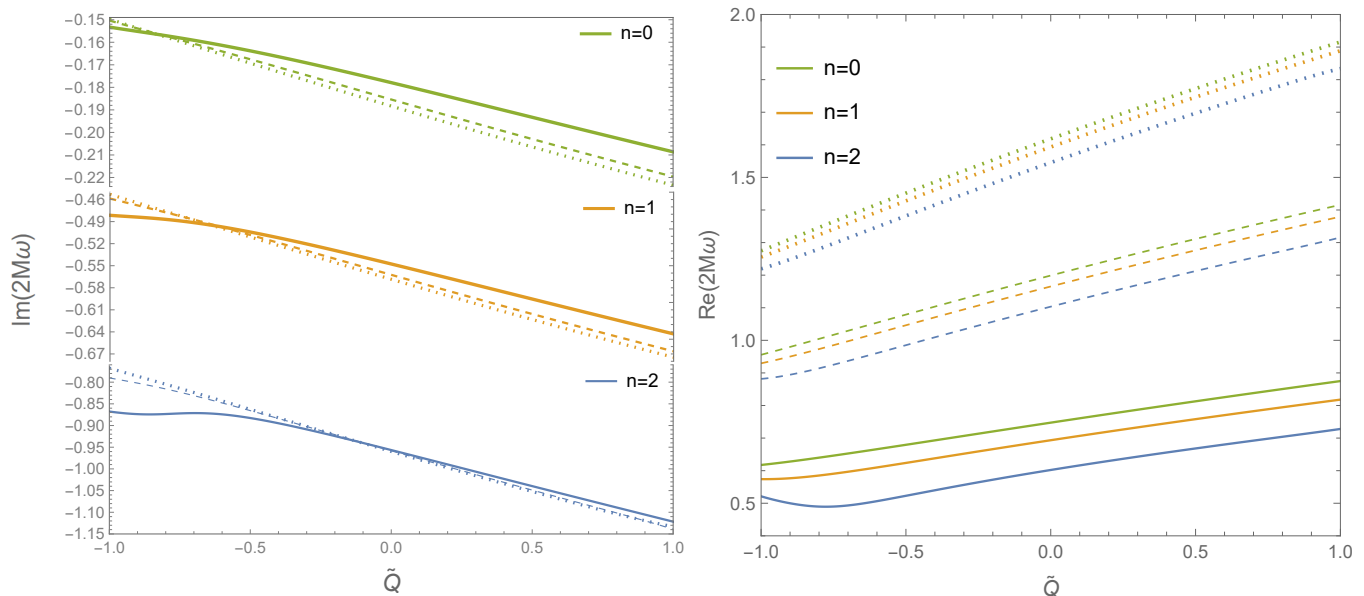


FIG. 2: The dimensionless QNMs as the functions of the hairy parameter  $Q$  for various modes. The different curves are denoted by the angular momenta  $\ell = 2$  (solid), 3 (dashed), 4 (dotted) and nodes  $n = 0$  (green), 1 (orange), 2 (blue), respectively.

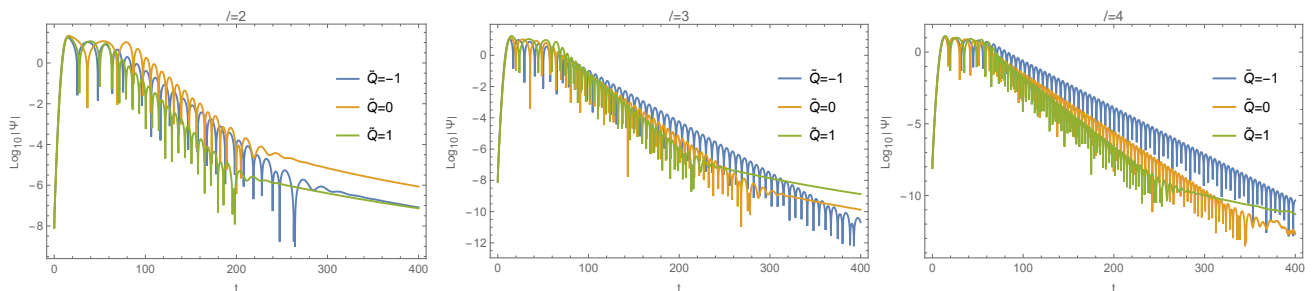


FIG. 3: The time evolution of the gravitational odd perturbation of the modes  $\ell = 2$  (left), 3 (middle), 4 (right) for selected hairy charge. The lifetime can be estimated by relating the amplitude with decay rate as  $\Psi \sim e^{-\alpha t}$ . In the above  $\log_{10}$  plots, the decay rate  $\alpha$  can be even intuitively inferred with the slope of the amplitude  $\log_{10} |\Psi| \sim -\alpha t$ . Therefore, the lifetime of a given mode is inversely proportional to the slope of its amplitude  $\tau \sim \frac{1}{\alpha}$  in the ringing stage. From the above plots, we observe that perturbations with a steeper slope have a shorter lifetime, and vice versa.

In our previous work [74], we have addressed the QNMs of massless scalar field, electromagnetic field and Dirac field around the Horndeski hairy black hole, so we collect those fundamental QNMs frequencies and the current QNMs of gravitational odd-parity perturbation into FIG.4 and shall discuss the effect of hairy parameter on how the QNMs depend on the field's spin. Our results show that for positive  $\tilde{Q}$ , the GW odd perturbation has the longest damping time and the strongest oscillation in their fundamental ( $n = 0$ ) and lowest-lying modes. However, as  $\tilde{Q}$  is approaching  $-1$ , the GW odd perturbation turns to the shortest-lived field. We argue that this phenomenon may attribute to the superluminal propagation of the odd perturbation especially for more negative hairy charge (see FIG. 1).

From the investigation on the QNMs, we find that the effect of the hairy parameter apparently differs the BH in Horndeski gravity from GR by significantly influencing the lifetime and the oscillation of gravitational odd perturbation. This will help to recognize and distinguish the hairy black hole in constructing the ringdown wave pattern and even constrain the hairy parameter in the ringdown observation. An interesting question comes follow and says that,

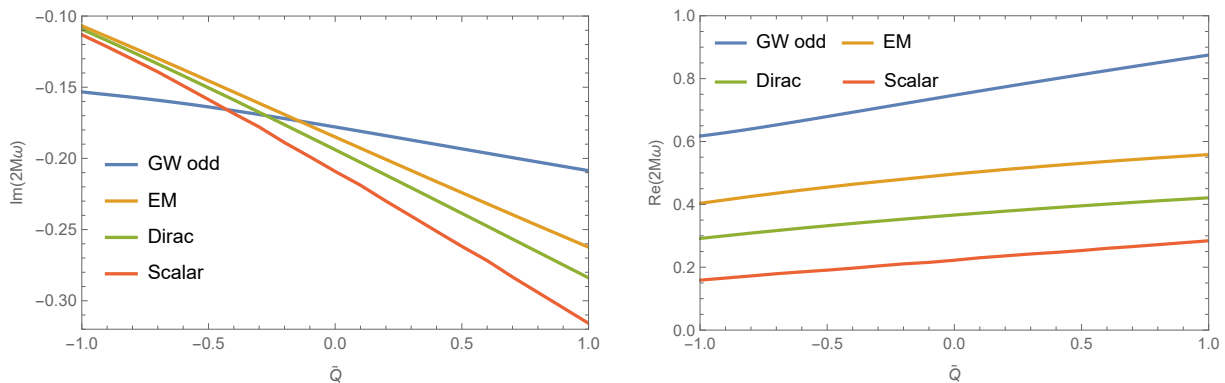


FIG. 4: The fundamental QNMs as the functions of the hairy parameter  $\tilde{Q}$ , for the perturbed massless scalar ( $s = 0, \ell = 0$ ), Dirac ( $s = 1/2, \ell = 1$ ), electromagnetic ( $s = 1, \ell = 1$ ) and GW odd ( $s = 2, \ell = 2$ ) fields.

base on the yielding QNMs data, to what extent can we constrain the horndeski BH hair according to the ringdown signal captured by GW interferometers. We will partly discuss this issue in next section.

#### IV. HAIRY PARAMETER ESTIMATION BY DETECTION OF RINGDOWN WAVE

In this section, we will determine the measurement errors of the hairy parameter  $\tilde{Q}$  by the GW detectors, which can be estimated by computing the Fisher information matrix (FIM) [79]. To this end, we shall follow the settings in [88] and start with a popular template of ringdown signals in GR

$$h = h_+ F_+ + h_\times F_\times, \quad (27)$$

where  $F_{+,\times}(\theta, \phi)$  are the detector pattern functions that depend on the propagation direction of the wave and the orientation of the detection plane. The strain functions  $h_{+,\times}(t)$  of two polarizations at ringdown stage are given by

$$h_+(t) = \sum_{\ell mn} A_{\ell mn}^+ e^{-\frac{\pi t f_{\ell mn}}{\mathcal{Q}_{\ell mn}}} S_{\ell mn} \cos(\phi_{\ell mn}^+ + 2\pi t f_{\ell mn}), \quad (28)$$

$$h_\times(t) = \sum_{\ell mn} A_{\ell mn}^\times e^{-\frac{\pi t f_{\ell mn}}{\mathcal{Q}_{\ell mn}}} S_{\ell mn} \sin(\phi_{\ell mn}^\times + 2\pi t f_{\ell mn}), \quad (29)$$

where  $\phi_{\ell mn}^{+,\times}$  and  $A_{\ell mn}^{+,\times}$  represent the phase angles and the reduced amplitudes that have encapsulated any constant normalization factors.  $S_{\ell mn}(\theta, \phi)$  denotes the spin-weighted spheroidal harmonics. The quality factors  $f_{\ell mn}$  and  $\mathcal{Q}_{\ell mn}$  are connected with the QNM frequency via

$$\omega_{QNM} = 2\pi f_{\ell mn} + \frac{i}{\tau_{\ell mn}}, \quad \mathcal{Q}_{\ell mn} = \pi f_{\ell mn} \tau_{\ell mn} \quad (30)$$

where  $f_{\ell mn}$  are the oscillation frequency, and  $\tau_{\ell mn}$  are related with the damping time. To begin with the error estimation under the detection of above waveform (27), we need to define a useful inner product  $(\cdot|\cdot)$ , weighted by a noise spectral density  $S_h(v)$  of a detector, between the signals  $h_1(t)$  and  $h_2(t)$ :

$$(h_1|h_2) \equiv 2 \int_0^\infty \frac{\tilde{h}_1^* \tilde{h}_2 + \tilde{h}_2^* \tilde{h}_1}{S_h(v)} dv, \quad (31)$$

with  $\tilde{h}(v)$  defined by the Fourier transformation of the waveform  $h(t)$ . Therefore the signal-to-noise-ratio (SNR) can now be defined as the self-inner product of a single waveform

$$\rho^2 = (h|h) = 4 \int_0^\infty \frac{\tilde{h}^*(v) \tilde{h}(v)}{S_h(v)} dv. \quad (32)$$

Then, for a given parameter space  $\{\theta_a\}$  associated with a template signal, one can estimate their errors with respect to measured signals by calculating the FIM

$$\Gamma_{ab} \equiv (\partial_a h | \partial_b h) \quad \text{with} \quad \partial_a \equiv \frac{\partial}{\partial \theta_a}. \quad (33)$$

Via inverting the FIM one obtains the covariance matrix and root-mean-square error for a single parameter

$$\Sigma_{ab} \equiv (\Gamma^{-1})_{ab} = \langle \Delta \theta_a \Delta \theta_b \rangle, \quad \sigma_a = \sqrt{\Sigma_{aa}} = \sqrt{\langle (\Delta \theta_a)^2 \rangle}. \quad (34)$$

For a preliminary work to perform parameter estimation, one usually impose some simplifying assumptions [79]:

(i). The wavelength of GWs is much larger than the arm length of interferometer, therefore, the spacial dependence of the signals can be neglected and hence the product of the pattern and spin-weighted functions appear in the angle averages as  $\langle F_+^2 \rangle = \langle F_\times^2 \rangle = 1/5$ ,  $\langle F_\times F_+ \rangle = 0$  and  $\langle |S_{\ell mn}|^2 \rangle = 1/4\pi$ .

(ii). Assume that the noise can be approximately seen as a constant over the bandwidth of the signals, so that we have  $\sigma_{\text{error}}^2 \sim S_h$  and  $\rho_{\text{SNR}}^2 \sim S_h^{-1}$ . So a natural way to get rid of the dependence of this constant noise is to multiply the error by SNR, i.e.  $\rho_{\text{SNR}} \sigma_{\text{error}}$ , which shall then represent a generic error re-scaled by SNR.

(iii). To further simplify the expression for SNR and error, one can define

$$A_{\ell mn}^\times = A_{\ell mn}^+ N_\times \quad (35)$$

$$\phi_{\ell mn}^\times = \phi_{\ell mn}^+ + \phi_{\ell mn}^0 \quad (36)$$

where the constant phase  $\phi_{\ell mn}^0$  and the numerical factor  $N_\times$  can be fixed because they are addressed to be less dependent on error [79].

We shall then concentrate our interest on the measurement error of the hairy parameter  $\tilde{Q}$  encoded within the QNMs frequencies  $\omega_{QNM}$  such that we have  $f_{\ell mn}(\tilde{Q})$  and  $\mathcal{Q}_{\ell mn}(\tilde{Q})$ . Since we are focusing on constraining a single parameter, so the Fisher matrix reduces to the ‘‘Fisher scalar’’  $\Gamma_{\tilde{Q}} = (\partial_{\tilde{Q}} h | \partial_{\tilde{Q}} h)$ . Recalling the aforementioned assumptions, the derivative on the waveform,  $\partial_{\tilde{Q}} h$ , is reflected in the derivatives on  $\partial_{\tilde{Q}} f_{\ell mn}$  and  $\partial_{\tilde{Q}} \mathcal{Q}_{\ell mn}$ . Since our QNMs frequencies related with  $\{f_{\ell mn}, \mathcal{Q}_{\ell mn}\}$  are obtained discretely, we shall do these derivatives numerically in computing the Fisher scalar as well as the errors of the hairy parameter. Consequently, for a fixed hairy parameter  $\tilde{Q}_0$ , the rescaled error  $\sigma_{\tilde{Q}_0}$  defined in this way describes the deviation from its best estimated value by the detectors. We shall evaluate the rescaled error of the hairy parameter by considering the signals composing of a single mode and two modes, respectively.

### A. Single-mode parameter estimation

Since our black hole is static and spherically symmetric, the odd gravitational perturbation equation here is independent of the azimuthal  $m$  [84], so we obviate  $m$  and consider the detecting signals are contributed only by a single mode with

$$h^+ = h_{n\ell}^+ = A^+ e^{-\frac{\pi t f_{n\ell}}{\mathcal{Q}_{n\ell}}} S_{n\ell} \cos(\phi^+ + 2\pi t f_{n\ell}), \quad (37)$$

$$h^\times = h_{n\ell}^\times = A^+ N_\times e^{-\frac{\pi t f_{n\ell}}{\mathcal{Q}_{n\ell}}} S_{n\ell} \sin(\phi^+ + \phi^0 + 2\pi t f_{n\ell}). \quad (38)$$

Here we set  $A^+ = \frac{A^2}{1+N_\times^2}$ , and  $\{N_\times = 1, \phi^+ = \phi^0 = 0\}$  for simplicity, and apply the formulas (31–34) laid out above, then the error (re-scaled by SNR) for a single-mode signal reads

$$\rho^2 \sigma_{\tilde{Q}}^2 \equiv \rho^2 \sigma_{n\ell}^2(\tilde{Q}) = \frac{2f_{n\ell}^2 \mathcal{Q}_{n\ell}^2}{f_{n\ell}^2 (\mathcal{Q}_{n\ell}^2 + 4\mathcal{Q}_{n\ell}^4) - 2f_{n\ell} \mathcal{Q}_{n\ell} f'_{n\ell} \mathcal{Q}'_{n\ell} + f_{n\ell}^2 \mathcal{Q}_{n\ell}^{\prime 2}}, \quad (39)$$

where the prime represents the derivative with respect to  $\tilde{Q}$ . As it was addressed in [89] that  $\Gamma^{-1}$  corresponds to the Cramer-Rao bound, which is a lower bound for the variance error of any unbiased parameter. So in our case the error

$\rho\sigma_{n\ell}(\tilde{Q})$  possesses the similar capability that describes a lower bound variance (re-scaled by SNR) on determining the source parameter  $\tilde{Q}$ . We compute the tendency of error as a function of hairy parameter  $\tilde{Q}$  for different single mode  $h_{n\ell}$ . As shown in FIG. 5, each curve describes a scaled lowest variance, which would be the best extent where the detector can constrain the hairy parameter in our setup. It can be clearly seen that the error bound of the hairy parameter becomes deeper as  $\ell$  increases but shallower as  $n$  increases, while the effect from the hairy parameter is relatively slight. In the figure, we also plot the errors for a large- $\mathcal{Q}$  approximation  $\rho^2\sigma_{n\ell}^2 \approx \frac{f_{n\ell}^2}{2f_{n\ell}^2\mathcal{Q}_{n\ell}^2}$  which is directly derived from (39). A direct comparison reveals that this approximation works better for the error estimation of the fundamental mode.

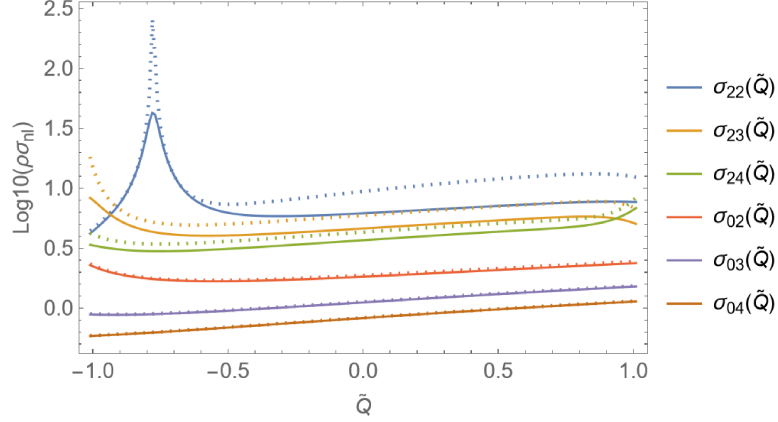


FIG. 5: The SNR-scaled error for single-mode  $h_{n\ell}$  measurements of hairy parameter  $\tilde{Q}$ , with various modes. The dotted curves are the errors from a large- $\mathcal{Q}$  approximation.

## B. Two-modes parameter estimation

The waveform mixed two different modes could be more significant in fitting astrophysical gravitational wave sources and testing the general no-hair theorem [79, 90, 91], so in this part we would like to discuss how the constraint response in considering the mixed waveforms. To model such signal, we consider the superposition of two QNMs with different  $\ell$  and  $n$ , which can be written as

$$h^+ = h_a^+ + h_b^+ = A_a^+ e^{-\frac{\pi t f_{n\ell}}{\mathcal{Q}_{n\ell}}} S_{n\ell} \cos(\phi_a^+ + 2\pi t f_{n\ell}) + (\ell \leftrightarrow \ell', n \leftrightarrow n', a \leftrightarrow b), \quad (40)$$

$$h^\times = h_a^\times + h_b^\times = A_a^+ N_\times e^{-\frac{\pi t f_{n\ell}}{\mathcal{Q}_{n\ell}}} S_{n\ell} \sin(\phi_a^+ + \phi_a^0 + 2\pi t f_{n\ell}) + (\ell \leftrightarrow \ell', n \leftrightarrow n', a \leftrightarrow b), \quad (41)$$

where for simplicity we have labeled the mode  $(\ell, n)$  as “a” and  $(\ell', n')$  as “b”. In dealing with the product of the angular scalar between two different modes, we follow the assumption from [79] that two close enough QNMs directly give

$$\int S_{n'\ell'}^* S_{n\ell} d\Omega \simeq \delta_{\ell'\ell}. \quad (42)$$

By setting  $\phi_a^+ = -\phi_a^0 = \phi_b^\times = \phi_b^0 = \frac{1}{2\pi}$ ,  $A_a^+ = A_a$ ,  $A_b^+ = A_b$  and  $N_\times = 1$ , we will obtain the SNR and the Fisher scalar as

$$\rho^2 = \rho_a^2 + \rho_b^2 + \delta_{\ell'\ell} \rho_c^2, \quad (43)$$

$$\Gamma_{\tilde{Q}} = \Gamma_{\tilde{Q}}^{(a)} + \Gamma_{\tilde{Q}}^{(b)} + \delta_{\ell'\ell} \Gamma_{\tilde{Q}}^{(c)}, \quad (44)$$

with

$$\rho_a^2 = \frac{A_a^2 \mathcal{Q}_{n\ell} (1 + \cos(\frac{1}{\pi}) + 8\mathcal{Q}_{n\ell}^2)}{\pi S_h f_{n\ell} (1 + 4\mathcal{Q}_{n\ell}^2)}, \quad \rho_b^2 = \frac{A_b^2 \mathcal{Q}_{n'\ell'} (2 + \cos(\frac{1}{\pi}) - \cos(\frac{1}{2\pi}) + 8\mathcal{Q}_{n'\ell'}^2)}{\pi S_h f_{n'\ell'} (1 + 4\mathcal{Q}_{n'\ell'}^2)}. \quad (45)$$

Here  $\{\rho_a, \Gamma_{\tilde{Q}}^{(a)}\}$  and  $\{\rho_b, \Gamma_{\tilde{Q}}^{(b)}\}$  denote the SNR and the Fisher scalar contributed by strains  $h_a$  and  $h_b$ , respectively, while  $\{\rho_c, \Gamma_{\tilde{Q}}^{(c)}\}$  represent the interacting term contributed by the product of two modes. We shall not present their expressions in details because of their complexity.

The appearing of delta symbol in (43) and (44) makes the hairy parameter estimation divide into two cases:

(i) When  $\ell' \neq \ell$  and  $n' = n$ , the cross term vanishes, so that the overall SNR and Fisher scalar become the sum in quadrature of two single modes and the scaled error are then expressed as

$$\rho^2 \sigma_{\tilde{Q}}^2 \equiv \rho^2 \sigma_{nab}^2(\tilde{Q}) = \frac{\rho_a^2 + \rho_b^2}{\Gamma_{\tilde{Q}}^{(a)} + \Gamma_{\tilde{Q}}^{(b)}}. \quad (46)$$

Here  $\sigma_{nab}$  denotes the variance of the mixed waveforms which have a same overtone but different angular numbers, for example,  $\sigma_{023}$  means the mix of the waveforms  $h_{02}$  and  $h_{03}$ . In this case, similar to that in single mode estimation, the mixed mode with same overtone but higher angular numbers possess lower errors as shown in the left panel of FIG.6. In order to discuss the subtle connections between the single mode and mixed mode estimation, we plot the middle and right panels of FIG.6 from which we can read off the following features: (1) when  $h_b = h_{n\ell'}$  dominates the mixed mode, i.e.,  $A_a/A_b < 1$ , the constraint becomes stronger and quickly approaches the single mode  $h_b$  itself (see the green curves). (2) when  $h_a = h_{n\ell}$  dominates the mixed mode, i.e.,  $A_a/A_b > 1$ , the constraint becomes weaker. Therefore, our results show that the measurement error from the mixed modes is rather sensitive to the their relative amplitude.

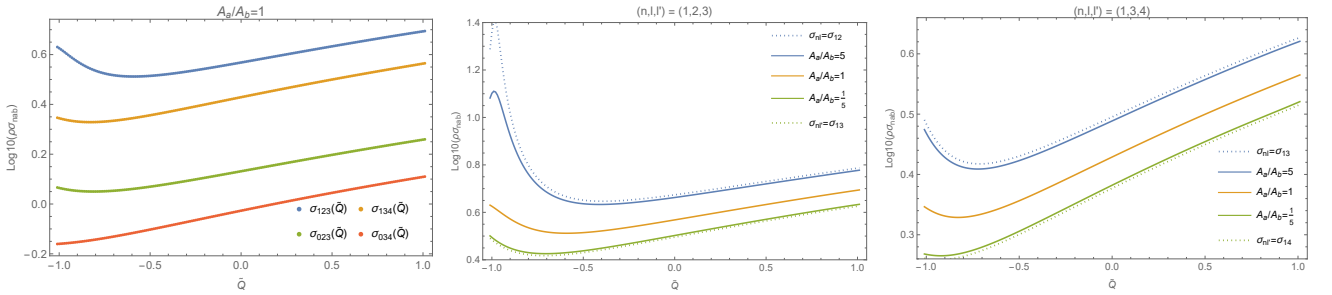


FIG. 6: The SNR-scaled error for two-modes  $\{h_a, h_b\} = \{h_{n\ell}, h_{n\ell'}\}$  measurements of hairy parameter  $\tilde{Q}$ , the single modes  $h_a$  and  $h_b$  share a same overtone but different angular numbers. In the left plot, we have  $(n, \ell, \ell') = (1, 2, 3)$  (blue),  $(1, 3, 4)$  (orange),  $(0, 2, 3)$  (green) and  $(0, 3, 4)$  (red), respectively. The middle and right plots present the error for the mixed modes  $(n, \ell, \ell') = (1, 2, 3)$  (middle) and  $(1, 3, 4)$  (right), but with different amplitude ratio  $A_a/A_b$  between the two modes. The dotted curves denotes the single-mode errors.

(ii) When  $\ell' = \ell$  and  $n' \neq n$ , the product of the scalar spherical harmonics (42) is approximated to unity, which introduce an additional term in overall SNR and Fisher scalar. Through straight algebraic calculations, we obtain the scaled error in this case as

$$\rho^2 \sigma_{\tilde{Q}}^2 \equiv \rho^2 \sigma_{\ell ab}^2(\tilde{Q}) = \frac{\rho_a^2 + \rho_b^2 + \rho_c^2}{\Gamma_{\tilde{Q}}^{(a)} + \Gamma_{\tilde{Q}}^{(b)} + \Gamma_{\tilde{Q}}^{(c)}}, \quad (47)$$

where  $\sigma_{\ell ab}$  denotes the variance of the mixed mode with the same angular number but different overtones, for example,  $\sigma_{201}$  mixes the waveforms  $h_{02}$  and  $h_{12}$ . The Key results are depicted in the left panel of FIG.7, showing that the mixed modes with same angular momentum but smaller overtones exhibit lower error. To more explicitly see the mixing effects, we plot the middle and right panels. The middle and right panels indicate that when the fundamental mode  $h_a = h_{n\ell}$  dominates the mixing, the overall error becomes smaller (see the green curves in middle and right panels of FIG.7), but if the next-to-leading overtone mode  $h_b = h_{n'\ell}$  dominates the mixed modes, the error becomes larger. In addition, due to the existence of the interacting term  $\Gamma_{\tilde{Q}}^{(c)}$ , we also observe intriguing phenomena that the detection potential from the mixed modes is not always better than that from the single mode, and it is significantly affected by the amplitude ratio  $A_a/A_b$  of the mixing mode as well as the hairy parameter.

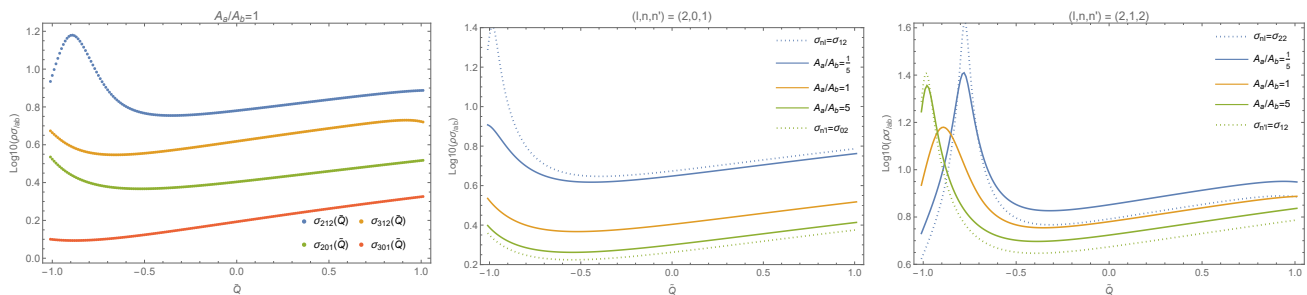


FIG. 7: The SNR-scaled error for two-modes  $\{h_a, h_b\} = \{h_{n\ell}, h_{n'\ell'}\}$  measurements of hairy parameter  $\tilde{Q}$ , the single modes  $h_a$  and  $h_b$  share a same angular number but different overtones. In the left plot, we have  $(\ell, n, n') = (2, 1, 2)$  (blue),  $(3, 1, 2)$  (orange),  $(2, 0, 1)$  (green),  $(3, 0, 1)$  (red), respectively. In the middle and right plots, we select the error with  $(\ell, n, n') = (2, 0, 1)$  (middle) and  $(2, 1, 2)$  (right) and check the effect of the amplitude ratio  $A_a/A_b = 1/5$  of the two modes. The dotted curves are the single-mode errors.

## V. CONCLUSIONS AND DISCUSSIONS

In this paper we have investigated how a specific Horndeski hair differ the QNMs of the black hole from GR in the context of gravitational odd perturbation, and intuitively analyzed the varying of QNMs with the hairy parameter by scrutinizing the evolution of the odd perturbation in time domain. Moreover, as a preliminary attempt, we used the yielding QNMs data to model ringdown waveforms of the hairy black hole and discussed the detectability of the hairy parameter, which was estimated from the Fisher information matrix for a single parameter. Our key findings are summarized as follows,

- The radial propagation speed of gravitation wave emitted by the remnant black hole in Horndeski gravity at the current setup is found to be  $c_r^2 = (1 + \frac{3Q}{2r})^{-1}$ , which is different from the vacuum light speed in GR. To avoid Laplacian instability, we obtained a constraint on the black hole hair as  $Q > -\frac{2}{3}r_+$ .
- Comparing to the Schwarzschild black hole in GR, we found that the odd perturbation in the specific Horndeski gravity is significantly influenced by the Horndeski hair. We mainly analyzed the influence of the hairy parameter on the QNMs frequencies. We found that in both frequency domain and time domain, the hairy black hole is dynamically stable under the odd perturbation. In particular, our results shew that when  $\tilde{Q}$  becomes negative enough, the leading mode becomes  $\ell > 2$  mode instead of  $\ell = 2$  mode, and also in this case the lifetime of the odd perturbation becomes the shortest one among all considered perturbations including massless scalar, Dirac, electromagnetic field perturbations. We argued that these phenomena may attribute to the superluminal propagation of the odd perturbation near the BH horizon, but the deeper physics deserves further study.
- In the context of parameter estimation by the ringdown waveform, we focused on the single parameter estimation of the Horndeski hair. Our results shew that the error bound of the mixed modes appeared in the average of the sum of corresponding single-mode errors. The ringdown observation would have a better constraint on the hairy parameter when the waveforms carry the larger  $\ell$  QNMs with smaller node  $n$ . The Horndeski black hole with negative  $\tilde{Q}$  was found to have a better constraint comparing to the cases with positive hairy charge. Furthermore, FIG.5-FIG.7 indicate that the rescaled measurement error of the hairy parameter is of order  $\mathcal{O}(1-10)$ . It means that the order of magnitude of the error on  $\tilde{Q}$  for different GW detectors is around  $\mathcal{O}(1-10)/\rho$  where  $\rho$  is the Ringdown SNR for the corresponding detector. It is also worth noting that toward the end of this work, we became aware of a recent paper [59] in which the authors forecast how GW experiments could constrain the scalar parameter of hairy black hole using only the fundamental  $\ell = 2$  ringdown mode extracted by the WKB method in scalar-tensor theory.

Based on our present findings on the QNMs of gravitational odd perturbation and the error estimation, a series of further work can be proceeded to make the studies more physically realistic. Firstly, as an extension of the current work

in the ringdown observation, a more comprehensive study on the parameter estimations, considering multi-parameters in the calculations of Fisher information matrix [77, 79, 90], will be a natural next step. We believe the covariance of general parameters (for instance, spins, masses, redshift, etc.) will produce more information about the detectability of a hairy black hole. Secondly, it is interesting to fit the ringdown wave form more realistically by imposing the non-linear modification [92] on the overtone model or considering the non-linear modes [93] in constructing the wave forms. Thirdly, other polarizations of gravitational wave modes may carry more interesting property on the observation of black hole spectroscopy (see for example [94–97]), and the effect of Horndeski hair on the GWs in EMRI system could be complementary to our current study. Those are worth to be studied for future work. The last but not the least, the extension of these studies to the gravitational even perturbation in the Horndeski gravity would be another challenging direction. The studies on all these topics could be significant for our understanding on the no-hair theorem and its testing via GW experiments.

### Acknowledgments

This work is partly supported by Natural Science Foundation of China under Grants No. 12375054 and the Postgraduate Research & Practice Innovation Program of Jiangsu Province under Grant No. KYCX23\_3501.

- 
- [1] B. P. Abbott et al. (LIGO Scientific, Virgo), *Phys. Rev. Lett.* **116**, 061102 (2016), 1602.03837.
  - [2] B. P. Abbott et al. (LIGO Scientific, Virgo), *Phys. Rev. X* **9**, 031040 (2019), 1811.12907.
  - [3] B. P. Abbott et al. (LIGO Scientific, Virgo), *Astrophys. J. Lett.* **892**, L3 (2020), 2001.01761.
  - [4] K. Akiyama et al. (Event Horizon Telescope), *Astrophys. J. Lett.* **875**, L1 (2019), 1906.11238.
  - [5] K. Akiyama et al. (Event Horizon Telescope), *Astrophys. J. Lett.* **930**, L12 (2022).
  - [6] A. E. Broderick, T. Johannsen, A. Loeb, and D. Psaltis, *Astrophys. J.* **784**, 7 (2014), 1311.5564.
  - [7] D. Psaltis, N. Wex, and M. Kramer, *Astrophys. J.* **818**, 121 (2016), 1510.00394.
  - [8] M. Khodadi, A. Allahyari, S. Vagnozzi, and D. F. Mota, *JCAP* **09**, 026 (2020), 2005.05992.
  - [9] M. Khodadi, G. Lambiase, and D. F. Mota, *JCAP* **09**, 028 (2021), 2107.00834.
  - [10] M. Tang and Z. Xu, *JHEP* **12**, 125 (2022), 2209.08202.
  - [11] E. Thrane, P. D. Lasky, and Y. Levin, *Phys. Rev. D* **96**, 102004 (2017), 1706.05152.
  - [12] M. Isi, M. Giesler, W. M. Farr, M. A. Scheel, and S. A. Teukolsky, *Phys. Rev. Lett.* **123**, 111102 (2019), 1905.00869.
  - [13] C. L. Rodriguez, I. Mandel, and J. R. Gair, *Phys. Rev. D* **85**, 062002 (2012), 1112.1404.
  - [14] A. Kuntz, R. Penco, and F. Piazza, *JCAP* **08**, 023 (2020), 2004.10772.
  - [15] A. Maselli, N. Franchini, L. Gualtieri, and T. P. Sotiriou, *Phys. Rev. Lett.* **125**, 141101 (2020), 2004.11895.
  - [16] L. G. Collodel, D. D. Doneva, and S. S. Yazadjiev, *Phys. Rev. D* **105**, 044036 (2022), 2108.11658.
  - [17] T.-G. Zi, J.-D. Zhang, H.-M. Fan, X.-T. Zhang, Y.-M. Hu, C. Shi, and J. Mei, *Phys. Rev. D* **104**, 064008 (2021), 2104.06047.
  - [18] H. Guo, Y. Liu, C. Zhang, Y. Gong, W.-L. Qian, and R.-H. Yue, *Phys. Rev. D* **106**, 024047 (2022), 2201.10748.
  - [19] D. Liang, R. Xu, Z.-F. Mai, and L. Shao, *Phys. Rev. D* **107**, 044053 (2023), 2212.09346.
  - [20] C. Zhang, Y. Gong, D. Liang, and B. Wang, *JCAP* **06**, 054 (2023), 2210.11121.
  - [21] T. Zi and P.-C. Li, *Phys. Rev. D* **108**, 084001 (2023), 2306.02683.
  - [22] H. Guo, C. Zhang, Y. Liu, R.-H. Yue, Y.-G. Gong, and B. Wang, *Chin. Phys. C* **48**, 095103 (2024), 2305.00652.
  - [23] I. Kamaretsos, M. Hannam, S. Husa, and B. S. Sathyaprakash, *Phys. Rev. D* **85**, 024018 (2012), 1107.0854.
  - [24] S. Gossan, J. Veitch, and B. S. Sathyaprakash, *Phys. Rev. D* **85**, 124056 (2012), 1111.5819.
  - [25] J. Meidam, M. Agathos, C. Van Den Broeck, J. Veitch, and B. S. Sathyaprakash, *Phys. Rev. D* **90**, 064009 (2014), 1406.3201.
  - [26] C. Shi, J. Bao, H. Wang, J.-d. Zhang, Y. Hu, A. Sesana, E. Barausse, J. Mei, and J. Luo, *Phys. Rev. D* **100**, 044036 (2019), 1902.08922.
  - [27] S. Bhagwat, X. J. Forteza, P. Pani, and V. Ferrari, *Phys. Rev. D* **101**, 044033 (2020), 1910.08708.
  - [28] G. W. Horndeski, *Int. J. Theor. Phys.* **10**, 363 (1974).
  - [29] E. Bellini, A. J. Cuesta, R. Jimenez, and L. Verde, *JCAP* **02**, 053 (2016), [Erratum: *JCAP* 06, E01 (2016)], 1509.07816.
  - [30] S. Bhattacharya and S. Chakraborty, *Phys. Rev. D* **95**, 044037 (2017), 1607.03693.
  - [31] C. D. Kreisch and E. Komatsu, *JCAP* **12**, 030 (2018), 1712.02710.
  - [32] S. Hou and Y. Gong, *Eur. Phys. J. C* **78**, 247 (2018), 1711.05034.
  - [33] A. Spurio Mancini, F. Köhlinger, B. Joachimi, V. Pettorino, B. M. Schäfer, R. Reischke, E. van Uitert, S. Brieden, M. Archidiacono, and J. Lesgourgues, *Mon. Not. Roy. Astron. Soc.* **490**, 2155 (2019), 1901.03686.
  - [34] A. Allahyari, M. A. Gorji, and S. Mukohyama, *JCAP* **05**, 013 (2020), [Erratum: *JCAP* 05, E02 (2021)], 2002.11932.
  - [35] R. Ghosh, S. Sk, and S. Sarkar, *Phys. Rev. D* **108**, L041501 (2023), 2306.14193.

- [36] T. Kobayashi, Rept. Prog. Phys. **82**, 086901 (2019), 1901.07183.
- [37] M. Rinaldi, Phys. Rev. D **86**, 084048 (2012), 1208.0103.
- [38] A. Cisterna and C. Erices, Phys. Rev. D **89**, 084038 (2014), 1401.4479.
- [39] X.-H. Feng, H.-S. Liu, H. Lü, and C. N. Pope, JHEP **11**, 176 (2015), 1509.07142.
- [40] T. P. Sotiriou and S.-Y. Zhou, Phys. Rev. Lett. **112**, 251102 (2014), 1312.3622.
- [41] Y.-G. Miao and Z.-M. Xu, Eur. Phys. J. C **76**, 638 (2016), 1607.06629.
- [42] X.-M. Kuang and E. Papantonopoulos, JHEP **08**, 161 (2016), 1607.04928.
- [43] E. Babichev, C. Charmousis, and A. Lehébel, Class. Quant. Grav. **33**, 154002 (2016), 1604.06402.
- [44] R. Benkel, T. P. Sotiriou, and H. Witek, Class. Quant. Grav. **34**, 064001 (2017), 1610.09168.
- [45] G. Filios, P. A. González, X.-M. Kuang, E. Papantonopoulos, and Y. Vásquez, Phys. Rev. D **99**, 046017 (2019), 1808.07766.
- [46] A. Cisterna, C. Erices, X.-M. Kuang, and M. Rinaldi, Phys. Rev. D **97**, 124052 (2018), 1803.07600.
- [47] A. Giusti, S. Zentarra, L. Heisenberg, and V. Faraoni, Phys. Rev. D **105**, 124011 (2022), 2108.10706.
- [48] A. Cisterna, M. Cruz, T. Delsate, and J. Saavedra, Phys. Rev. D **92**, 104018 (2015), 1508.06413.
- [49] A. Anabalón, A. Cisterna, and J. Oliva, Phys. Rev. D **89**, 084050 (2014), 1312.3597.
- [50] R. D. B. Fontana, J. de Oliveira, and A. B. Pavan, Eur. Phys. J. C **79**, 338 (2019), 1808.01044.
- [51] E. Babichev and C. Charmousis, JHEP **08**, 106 (2014), 1312.3204.
- [52] E. Babichev, C. Charmousis, G. Esposito-Farèse, and A. Lehébel, Phys. Rev. Lett. **120**, 241101 (2018), 1712.04398.
- [53] J. Ben Achour and H. Liu, Phys. Rev. D **99**, 064042 (2019), 1811.05369.
- [54] K. Takahashi, H. Motohashi, and M. Minamitsuji, Phys. Rev. D **100**, 024041 (2019), 1904.03554.
- [55] M. Minamitsuji and J. Edholm, Phys. Rev. D **100**, 044053 (2019), 1907.02072.
- [56] N. Arkani-Hamed, P. Creminelli, S. Mukohyama, and M. Zaldarriaga, JCAP **04**, 001 (2004), hep-th/0312100.
- [57] J. Khoury, M. Trodden, and S. S. C. Wong, JCAP **11**, 044 (2020), 2007.01320.
- [58] A. Bakopoulos, C. Charmousis, P. Kanti, N. Lecoer, and T. Nakas, Phys. Rev. D **109**, 024032 (2024), 2310.11919.
- [59] S. Sirera and J. Noller (2024), 2408.01720.
- [60] S. Mironov, M. Sharov, and V. Volkova (2024), 2408.01480.
- [61] L. Hui and A. Nicolis, Phys. Rev. Lett. **110**, 241104 (2013), 1202.1296.
- [62] E. Babichev, C. Charmousis, and A. Lehébel, JCAP **04**, 027 (2017), 1702.01938.
- [63] S. E. P. Bergliaffa, R. Maier, and N. d. O. Silvano (2021), 2107.07839.
- [64] R. K. Walia, S. D. Maharaj, and S. G. Ghosh, Eur. Phys. J. C **82**, 547 (2022), 2109.08055.
- [65] F. Atamurotov, F. Sarikulov, A. Abdujabbarov, and B. Ahmedov, Eur. Phys. J. Plus **137**, 336 (2022).
- [66] J. Kumar, S. U. Islam, and S. G. Ghosh, Eur. Phys. J. C **82**, 443 (2022), 2109.04450.
- [67] M. Afrin and S. G. Ghosh, Astrophys. J. **932**, 51 (2022), 2110.05258.
- [68] S. Vagnozzi et al., Class. Quant. Grav. **40**, 165007 (2023), 2205.07787.
- [69] S. K. Jha, M. Khodadi, A. Rahaman, and A. Sheykhi (2022), 2212.13051.
- [70] Y.-H. Lei, Z.-H. Yang, and X.-M. Kuang, Eur. Phys. J. C **84**, 438 (2024), 2310.05190.
- [71] X.-J. Wang, X.-M. Kuang, Y. Meng, B. Wang, and J.-P. Wu, Phys. Rev. D **107**, 124052 (2023), 2304.10015.
- [72] S. Hu, D. Li, C. Deng, X. Wu, and E. Liang (2023), 2309.10557.
- [73] H.-Y. Lin and X.-M. Deng, Eur. Phys. J. C **83**, 311 (2023).
- [74] Z.-H. Yang, Y.-H. Lei, X.-M. Kuang, and J.-P. Wu, Eur. Phys. J. C **84**, 153 (2024), 2309.03565.
- [75] E. Berti et al., Class. Quant. Grav. **32**, 243001 (2015), 1501.07274.
- [76] H.-P. Nollert, Class. Quant. Grav. **16**, R159 (1999).
- [77] E. Berti, V. Cardoso, and A. O. Starinets, Class. Quant. Grav. **26**, 163001 (2009), 0905.2975.
- [78] R. A. Konoplya and A. Zhidenko, Rev. Mod. Phys. **83**, 793 (2011), 1102.4014.
- [79] E. Berti, V. Cardoso, and C. M. Will, Phys. Rev. D **73**, 064030 (2006), gr-qc/0512160.
- [80] T. Kobayashi, H. Motohashi, and T. Suyama, Phys. Rev. D **85**, 084025 (2012), [Erratum: Phys.Rev.D 96, 109903 (2017)], 1202.4893.
- [81] T. Kobayashi, H. Motohashi, and T. Suyama, Phys. Rev. D **89**, 084042 (2014), 1402.6740.
- [82] T. Regge and J. A. Wheeler, Phys. Rev. **108**, 1063 (1957).
- [83] A. De Felice, T. Suyama, and T. Tanaka, Phys. Rev. D **83**, 104035 (2011), 1102.1521.
- [84] A. Ganguly, R. Gannouji, M. Gonzalez-Espinoza, and C. Pizarro-Moya, Class. Quant. Grav. **35**, 145008 (2018), 1710.07669.
- [85] Z. Zhu, S.-J. Zhang, C. E. Pellicer, B. Wang, and E. Abdalla, Phys. Rev. D **90**, 044042 (2014), [Addendum: Phys.Rev.D 90, 049904 (2014)], 1405.4931.
- [86] A. Jansen, Eur. Phys. J. Plus **132**, 546 (2017), 1709.09178.
- [87] K. Lin and W.-L. Qian, Chin. Phys. C **43**, 035105 (2019), 1902.08352.
- [88] S. S. Lahoz and J. Noller, Phys. Rev. D **107**, 124054 (2023), 2301.10272.
- [89] M. Vallisneri, Phys. Rev. D **77**, 042001 (2008), gr-qc/0703086.
- [90] E. Berti, V. Cardoso, and C. M. Will, AIP Conf. Proc. **848**, 687 (2006), gr-qc/0601077.
- [91] L. Barack and C. Cutler, Phys. Rev. D **69**, 082005 (2004), gr-qc/0310125.
- [92] Y. Qiu, X. J. Forteza, and P. Mourier, Phys. Rev. D **109**, 064075 (2024), 2312.15904.
- [93] N. Khera, A. Ribes Metidieri, B. Bonga, X. Jiménez Forteza, B. Krishnan, E. Poisson, D. Pook-Kolb, E. Schnetter, and H. Yang, Phys. Rev. Lett. **131**, 231401 (2023), 2306.11142.
- [94] P. S. Barbeau, J. I. Collar, and O. Tench, JCAP **09**, 009 (2007), nucl-ex/0701012.
- [95] M. Rakhmanov, Phys. Rev. D **71**, 084003 (2005), gr-qc/0406009.
- [96] A. Nishizawa, A. Taruya, K. Hayama, S. Kawamura, and M.-a. Sakagami, Phys. Rev. D **79**, 082002 (2009), 0903.0528.



[97] Y. Gong and S. Hou, EPJ Web Conf. **168**, 01003 (2018), 1709.03313.